

See discussions, stats, and author profiles for this publication at: <https://www.researchgate.net/publication/237015597>

A Quasi-Quantum Well Sensitized Solar Cell with Accelerated Charge Separation and Collection

ARTICLE in JOURNAL OF THE AMERICAN CHEMICAL SOCIETY · JUNE 2013

Impact Factor: 12.11 · DOI: 10.1021/ja403756s · Source: PubMed

CITATIONS

43

READS

34

7 AUTHORS, INCLUDING:



Keyou Yan

The Chinese University of Hong Kong

49 PUBLICATIONS 1,394 CITATIONS

SEE PROFILE



Lixia Zhang

The Hong Kong University of Science and Tec...

57 PUBLICATIONS 647 CITATIONS

SEE PROFILE



Yongcai Qiu

Stanford University

73 PUBLICATIONS 2,614 CITATIONS

SEE PROFILE



Shihe Yang

The Hong Kong University of Science and Tec...

381 PUBLICATIONS 11,332 CITATIONS

SEE PROFILE

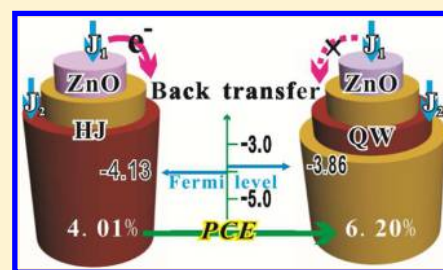
A Quasi-Quantum Well Sensitized Solar Cell with Accelerated Charge Separation and Collection

Keyou Yan,[†] Lixia Zhang,[‡] Jianhang Qiu,[†] Yongcai Qiu,[†] Zonglong Zhu,[†] Jiannong Wang,[‡] and Shihe Yang^{*†}

[†]Nano Science and Technology Program, Department of Chemistry and [‡]Department of Physics, The Hong Kong University of Science and Technology, Clear Water Bay, Kowloon, Hong Kong

S Supporting Information

ABSTRACT: Semiconductor-sensitized solar cell (SSSC) represents a new generation of device aiming to achieve easy fabrication and cost-effective performance. However, the power of the semiconductor sensitizers has not been fully demonstrated in SSSC, making it actually overshadowed by dye-sensitized solar cell (DSSC). At least part of the problem is related to the inefficient charge separation and severe recombination with the current technologies, which calls on rethinking about how to better engineer the semiconductor sensitizer structure in order to enhance the power conversion efficiency (PCE). Herein we report on using for the first time a quasi-quantum well (QW) structure (ZnSe/CdSe/ZnSe) as the sensitizer, which is quasi-epitaxially deposited on ZnO tetrapods. Such a novel photoanode architecture has attained 6.20% PCE, among the highest reported to date for this type of SSSCs. Impedance spectra have revealed that the ZnSe/CdSe/ZnSe QW structure has a transport resistance only a quarter that of, but a recombination resistance twice that of the ZnSe/CdSe heterojunction (HJ) structure, yielding much longer electron diffusion length, consistent with the resulting higher photovoltage, photocurrent, and fill factor. Time-resolved photoluminescence spectroscopy indicates dramatically reduced electron transfer from ZnO to the QW sensitizer, a feature which is conducive to charge separation and collection. This study together with the impedance spectra and intensity modulated photocurrent spectroscopies supports a core/shell two-channel transport mechanism in this type of solar cells and further suggests that the electron transport along sensitizer can be considerably accelerated by the QW structure employed.



INTRODUCTION

The efficient extraction of energy from solar radiation is one of the most attractive approaches to meet the societal needs as it is clean and renewable. Semiconductor sensitizers in the form of quantum dots (QD) or extremely thin absorber (ETA) layers can be facily tailored for efficient light harvesting (high extinction coefficient and wide absorption range).^{1,2} Such light harvesting capability coupled with the possibility of multiple exciton generation and hot carrier extraction through size control and composition management makes semiconductor sensitizers strong contenders to the traditional, organic dye chromospheres for the new generation of solar cells.^{3–14} Recently, the development of solution unstable (or soluble) semiconductor solar cells has been accelerated and new power conversion efficiency (PCE) records have been attained. For example, Sb₂S₃-sensitized mesoscopic TiO₂ solar cells (or ETA variety),^{15–22} although the constituent Sb₂S₃ is alcohol soluble and reactive toward polysulfide liquid electrolyte, reached a PCE of 6.3% when P3HT/PCBM was used as a hole transporter, which is actually the donor–acceptor system used in polymer solar cells.¹⁷ Strikingly, a high PCE of 9.7% has been achieved with (CH₃NH₃)PbI₃ perovskite nanocrystals as the light absorber and spiro-MeOTAD as the hole-transporting layer.²³ Higher PCE of 10.9% was further delivered by replacing the mesoporous n-type TiO₂ with

insulating Al₂O₃ superstructure under full sun illumination.²⁴ However, the solubility of this type of sensitizers^{25,26} is thought to limit the performance stability and the device reproducibility because of the ineluctable sensitizer leakage, which also could cause lead pollution problems beyond recycling for environmental conservation.

Until now, the solution stable CdS and CdSe QD-sensitized solar cells are still grappling with the 5% PCE barrier^{27–29} and further developments down the road call for new effective strategies to enhance open-circuit voltage (V_{oc}), short-circuit current (J_{sc}), and fill factor (FF). Recent efforts to improve PCE of such cells included the use of double layered electrodes,³⁰ improved anchorage of QDs,³¹ cosensitization with other QDs^{30,32–35} or dyes,^{36,37} and doping method.²⁷ Some work has extended the semiconductor sensitizer to other types of nanostructures for efficient charge collection, such as quantum rods.^{38,39} However, quantum wells (QWs),^{40–44} a typical two-dimensional (2D) confined quantum structure potentially having superior electron transport and collection properties, have not been explored to sensitize low-cost solar cells partly due to the difficulties involved in fabricating such a well-defined structure on a commonly used mesoscopic

Received: April 16, 2013

Published: June 3, 2013

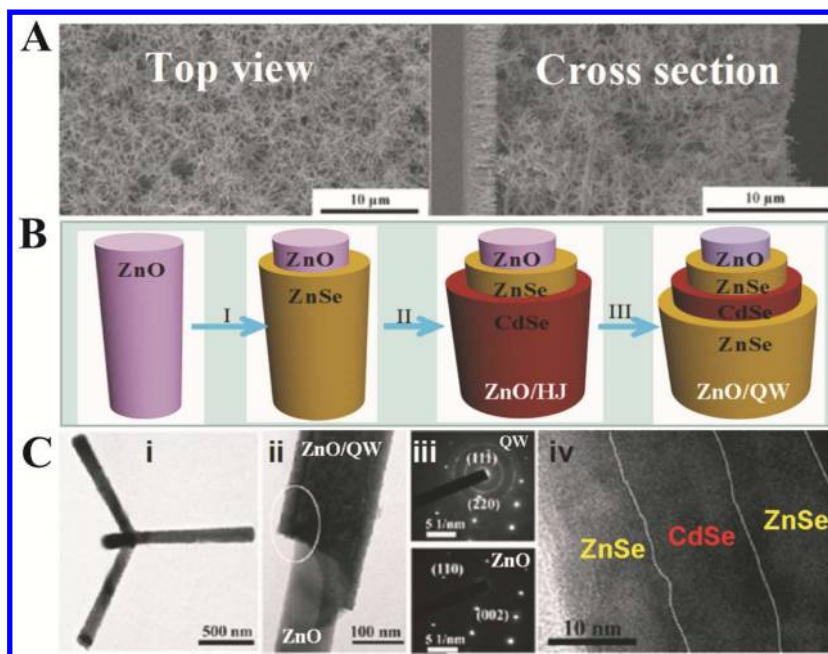


Figure 1. Layer by layer formation of the ZnSe/CdSe/ZnSe QW sensitizer. (A) Top and cross-sectional view SEM images of ZnO nanotetrapods photoanode for SSSCs. (B) Schematic diagram of the formation process: (i) Place the photoanode in freshly prepared NaHSe; (ii) dip in Cd^{2+} and NaHSe solution successively for four cycles; (iii) dip in Zn^{2+} and NaHSe solution successively for two cycles. (C) TEM images of QW-sensitized tetrapod, the arm apart from tetrapod and electron diffractions corresponding to different sections with and without QW shell and structure.

photoanode film. In the present work, through nanostructural engineering, we have developed a quasi-QW sensitizer of a tubular ZnSe/CdSe/ZnSe nanostructure accreted in a controlled fashion on tetrapod-like ZnO rods, gaining about 6.20% PCE, much higher than that of a control cell with a designated type II heterojunction (HJ) of ZnSe/CdSe on ZnO (4.01%). Even though it is only a rudimentary emulation of a *bona fide* QW through wet chemical processing, electrochemical impedance spectroscopy (EIS) has revealed much faster electron transport and much lesser recombination, resulting in more efficient charge collection, of the QW structure than the HJ structure. Besides, time-resolved photoluminescence spectroscopy (TRPL) has demonstrated dramatically reduced PL quenching in the ZnO/QW structure arising from electron transfer from ZnO to CdSe compared to the control structure of ZnO/HJ, indicating superior charge separation and collection of ZnO/QW.

RESULTS AND DISCUSSION

Structure Characterization. Figure 1 establishes the layer-by-layer formation of the ZnSe/CdSe/ZnSe QW sensitizer. From the top and cross section views (Figure 1A) of the double layer based photoanode employed for the semiconductor-sensitized solar cells (SSSCs), one can see that the top ZnO tetrapods and the underlying ZnO nanorod array are well organized and closely interwoven. Laid out in Figure 1B schematically is the synthesis procedure of the QW structure. Since surface anions of ZnO could be facily exchanged with Se^{2-} , a more stable ZnSe shell with ~ 15 nm thickness was formed yielding a core/shell tetrapod after Step I (labeled as ZnO/ZnSe). In Step II, the ZnSe shell was partially converted to CdSe through ion replacement of Zn^{2+} by Cd^{2+} , followed by quasi-epitaxial growth of CdSe through successive dipping in NaHSe and Cd^{2+} solutions (labeled as ZnO/HJ). In Step III, using the same procedure, the outmost ZnSe shell was formed

(shortened as ZnO/QW). During each dipping, the photoanode was rinsed with water to remove excess ions. Figure 1C (i) and (ii) clearly demonstrates that the final QW tube was seamlessly coated on the ZnO tetrapods. From the electron diffraction patterns (see Figure 1C (iii)) of two different parts of a tetrapod arm with the QW coating but partially peeled off (see Figure 1C (ii)), we can see that the single crystalline ZnO is conformally surrounded by a quasi-QW, namely a close-fitting, polycrystalline ZnSe/CdSe/ZnSe tube. In Figure 1C (iv), we have approximately marked off the two ZnSe shells (about 8–10 nm each) that sandwich the CdSe shell (about 10 nm) (see details in Figure S1).

In order to elucidate the structures of HJ and QW, the ZnO cores were removed with acetic acid, leaving behind only the HJ and QW nanotubes. Figure 2 displays the energy-dispersive X-ray spectroscopy (EDS) line scan curves of those HJ and QW nanotubes for Zn, Cd, and Se elementals, along with the corresponding scanning transmission electron microscope (STEM) images in the insets. Aside from the common tubular feature dictated by the overall hollow structure, outer shells clearly differ, manifesting the formation of HJ (ZnSe/CdSe) and QW (ZnSe/CdSe/ZnSe), respectively. More specifically, from the composition profiles along with the Raman spectra to be presented below, we can find that the QW layer is Cd-rich, sandwiched by the Zn-rich shells, whereas the Cd-rich layer in HJ is the outermost shell separated from the core by the ZnSe shell. Besides, from the composition profiles, we can see that a transitional $\text{Cd}_x\text{Zn}_{1-x}\text{Se}$ layer is formed at the interface between ZnSe and CdSe, which can help to reduce the lattice mismatch strain and thus form the close-fitting core/shell structure. Corresponding to the compositional profiles in the heterostructures, the energy band gap profiles have been deduced with a bowing factor of 0.67^{45,46} (see details in Supporting Information) and the results are shown in Figure 2C,D. Since the valence band (VB) offset between ZnSe and CdSe is negligible (see Figure S2), the energy band gap profiles in

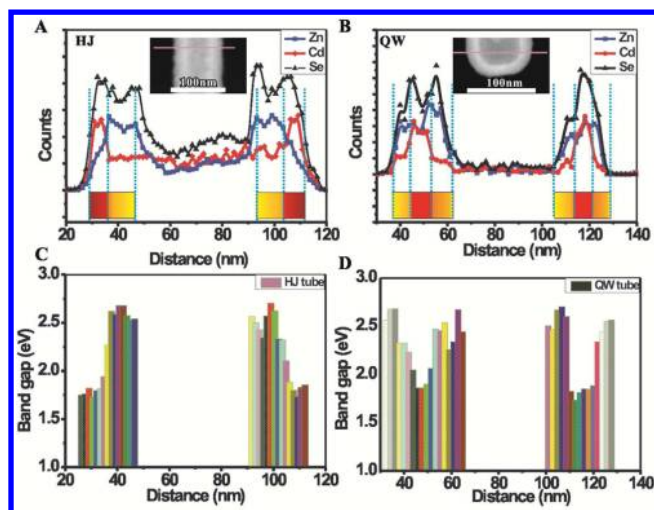


Figure 2. EDS line scan profiles of the sensitizer structure. STEM images (insets) and EDS line-scan analyses of (A) one HJ tube sensitizer and (B) one QW tube sensitizer; (blue dashed lines roughly separate elemental distribution domains of CdSe and ZnSe, red squares denote CdSe, and yellow squares denote ZnSe). The roughly estimated band gap profile as a function of position in (C) HJ and (D) QW nanotubes.

Figure 2C,D essentially reflects the conduction band (CB) edge profiles of HJ and QW, which are very useful for the discussion below embodied in Figure S4.⁴⁵ Further characterization includes the room-temperature Raman spectra of bare ZnO, ZnO/HJ, and ZnO/QW based photoanode, which are shown in Figure S3. In the Raman spectrum of bare ZnO, a peak of the zone-boundary phonon E_2 mode (E_2 -ZnO) at $\sim 438\text{ cm}^{-1}$ is observed, which is a characteristic of wurtzite ZnO.⁴⁷ For the spectra of ZnO/HJ and ZnO/QW, in addition to the E_2 -ZnO mode with a small shift to $\sim 430\text{ cm}^{-1}$, Raman peaks at ~ 233 and $\sim 204\text{ cm}^{-1}$ arising from the first-order longitudinal optical phonon mode of ZnSe (LO-ZnSe) and CdSe (LO-CdSe) are observed, consistent with the formation of the ZnSe and CdSe shells in the HJ and QW mentioned above.⁴⁸ It is instructive to compare the Raman spectra of ZnO/HJ and ZnO/QW. The Raman peak of ZnO/QW shows an increase in intensity of LO-ZnSe with respect to that of ZnO/HJ, in concurrence with the additional layer of ZnSe that caps the ZnO/HJ.

Photovoltaic (PV) Performance Evaluation. Figure 3 shows PV performance, including J - V curves, light harvest capability, and incident photon to current conversion efficiencies (IPCE), of the two types of solar cells, the ZnO/QW and ZnO/HJ variants, both using the GO/Cu₂S counter electrode and PEG gelled polysulfide electrolyte. The extracted cell performance parameters from Figure 3A are tabularized in Table 1 along with those of the same solar cells but using Pt counter electrode (see Figure S4). The HJ-sensitized solar cell registered a J_{sc} of 15.2 mA cm^{-2} , V_{oc} of 0.703 V , and FF of 37.4%, leading to a PCE of 4.02%. This is about the average performance of ZnO based SSSCs at present. However, after the outmost ZnSe coating to form the so-called ZnO/QW, the corresponding cells acquired J_{sc} of 17.3 mA cm^{-2} , V_{oc} of 0.761 V , and FF of 47.1%, yielding a 6.20% PCE. The FF is smaller when Pt was used as the counter electrode because of the corresponding large charge-transfer resistance with the polysulfide electrolyte⁴⁹ (also see Figure S5). Figure 3B shows UV-vis diffuse reflectance spectra of bare ZnO, ZnO/HJ, and ZnO/QW based photoanodes, which inform on their

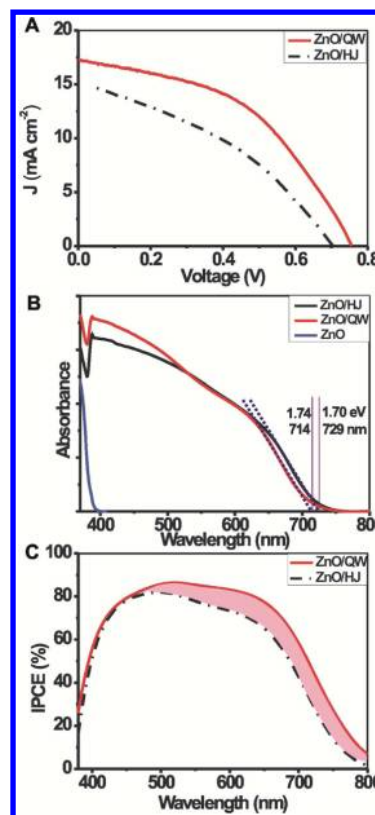


Figure 3. Performance evaluation of the ZnO/QW and ZnO/HJ solar cells. (A) The J - V characteristics. (B) Light harvest capability characteristics extracted from diffuse reflectance spectra. (C) IPCE curves: pink hatched region indicates the photoconversion improvement from ZnO/HJ to ZnO/QW.

light harvest capabilities. The absorption edge of each sample was estimated from the intersection point of the tracing dashed line with the x -axis (indicated by the vertical line, see Figure 3B). It is worth mentioning, that after the outmost coating of ZnSe that transformed HJ to QW, although the absorbance increases at the shorter wavelengths than 500 nm, the absorption edge is blue-shifted by 15 nm from 729 to 714 nm (as marked in Figure 3B), resulting in a somewhat reduced light harvest capability. The IPCEs as a function of wavelength for ZnO/HJ and ZnO/QW are shown in Figure 3C, which tally well with photocurrent of J - V curves. Even though the ZnO/HJ cell absorbs more strongly than the ZnO/QW cell in the long wavelength region $>500\text{ nm}$ (see the absorption spectrum in Figure 3B), the corresponding IPCE curve of ZnO/HJ actually lies below that of ZnO/QW (highlighted by the hatched pink area in Figure 3C). This clearly shows that the outmost ZnSe shell has contributed to the enhancement of the electron collection and/or the electron injection from the CdSe shell especially in the longer wavelength region, according to the relation: $\text{IPCE} = \text{LHE} \times \eta_{cc} \times \eta_{in}$ (LHE: light harvest efficiency; η_{cc} : charge collection efficiency; η_{in} : electron injection efficiency).

Dynamic Electrochemistry. In order to give a reasonable interpretation on the superior performance of the QW-sensitized solar cell, EIS was first employed to gain the dynamic information on charge transport and recombination, and the results are shown in Figure 4. Generally, from high to low frequency, the features successively represent electron diffusion in mesoporous films (about 10 M to 10 K Hz),

Table 1. Performance Parameters of the ZnO/HJ and ZnO/QW Solar Cells

solar cells	counter electrode	V_{oc} (V)	J_{sc} (mA cm ⁻²)	FF (%)	PCE (%)
ZnO/HJ	Pt	0.712 ± 0.012	15.3 ± 0.5	29.6 ± 3.1	3.22 ± 0.41
	GO/Cu ₂ S	0.703 ± 0.011	15.2 ± 0.4	37.4 ± 2.3	4.01 ± 0.52
ZnO/QW	Pt	0.741 ± 0.013	17.8 ± 0.5	39.8 ± 2.9	5.25 ± 0.33
	GO/Cu ₂ S	0.761 ± 0.011	17.3 ± 0.6	47.1 ± 2.2	6.20 ± 0.42

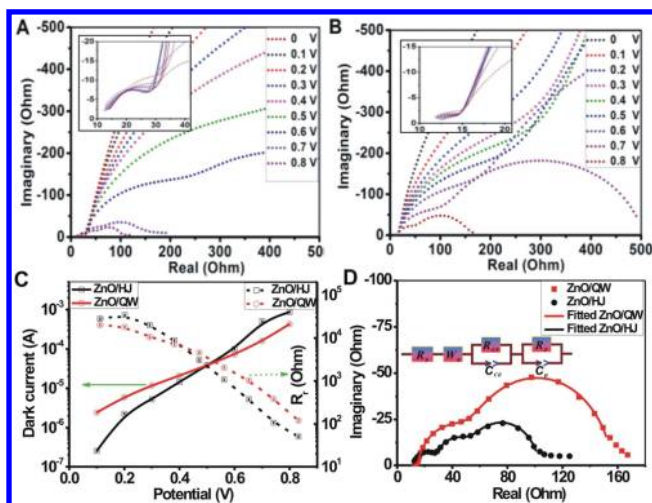


Figure 4. EIS measurements of the ZnO/HJ and ZnO/QW solar cells. (A) Nyquist plots of ZnO/HJ solar cell at different bias in the dark. (B) Nyquist plots of ZnO/QW solar cell at different bias in the dark (inset in A and B: magnification at highest frequencies). (C) Dark currents during the IS measurements and fitted recombination resistance for ZnO/HJ and ZnO/QW solar cells. (D) Model (inset) fitted Nyquist plots of ZnO/HJ and ZnO/QW solar cells at 0.8 V forward bias (fitted parameters shown in Table 2).

charge-transfer resistance at counter electrode (about 100 K to 1 K Hz), recombination resistance (about 1 K to 10 Hz) at mesoporous interface and redox couple shuttle diffusion (about 10 to 0.1 Hz).^{50,51} The data can be fitted with the equivalent circuit model presented in the inset of Figure 4D using finite length Warburg-short circuit terminus (W_s) to depict electron transport (R_t) in mesoporous film, R_{CE} shunted with C_{CE} to reflect charge-transfer process of counter electrode, and R_r shunted with C_r to reflect recombination process that takes place in the device. Figure 4A,B displays respective Nyquist plots of HJ and QW under different forward bias in the dark manifesting the various charge transfer events mentioned above, and the insets highlight the transport impedance of the mesoporous films in the highest frequency region. From the insets of Figure 4, one can see that ZnO/QW exhibits much smaller R_t than the control structure of ZnO/HJ at different forward bias voltages, demonstrating much more fluent electron transport in ZnO/QW than in ZnO/HJ. The dark currents at different forward bias in the EIS measurement are displayed as a solid line in Figure 4C. One can see that the EIS dark current of ZnO/QW solar cell is not as steep as that of ZnO/HJ solar cells, suggesting better blockage of charge recombination. The

better hindered recombination is also reflected in the recombination resistance (R_r) measurement (right y-axis in Figure 4C, dashed lines), from which R_r was extracted by fitting the data to the equivalent circuit model in the inset of Figure 4D. When the forward bias is larger than 0.4 V, the R_r values of ZnO/QW solar cell are several times those of ZnO/HJ solar cell. Specially, Figure 4D gives direct comparison of ZnO/QW and ZnO/HJ solar cells at 0.8 V in the dark. One can see from the fitted values, that the ZnO/QW solar cell has only one-fourth of the transport resistance but twice the recombination resistance of ZnO/HJ solar cells, yielding a much larger diffusion length (L_n) for ZnO/QW (125.0 μ m) than for ZnO/HJ (41.5 μ m) and consequently demonstrating much better charge collection efficiency of ZnO/QW solar cell.

The better charge transport of ZnO/QW than ZnO/HJ can be explained in the framework of the two-channel transport mechanism. Because there is a compact layer of semiconductor sensitizers, the electrons could transport through two channels: the sensitizer channel plus the conventional ZnO channel. In such a two-channel transport mechanism proposed here to account for the EIS result, the electron transport capability within the ZnO based skeleton can be considered to be the same in ZnO/HJ and in ZnO/QW. Thus the whole difference in transport between ZnO/QW and ZnO/HJ should really arise from their different structures: HJ and QW. Further support for the two transport channels comes from intensity modulated photocurrent spectroscopy (IMPS), which probes the charge transport characteristics with a dc light source modulated by a weak ac light. Surprisingly, we found two distinct resonance peaks in both ZnO/HJ and ZnO/QW, as shown in Figure 5A,B, which are compelling evidence for the two charge transport channels. We assign the high frequency peak (better charge transport) as ZnO channel and the low frequency one as HJ (or QW) channel because single crystalline ZnO is expected to have higher electron mobility than the polycrystalline HJ and QW. More interesting are the differences of the IMPS between ZnO/HJ and ZnO/QW. Obviously, the IMPS response of ZnO/QW is generally larger than that of ZnO/HJ (see Figure 5A,B), which is consistent with larger J_{sc} produced by QW than HJ. The diffusion coefficients deduced from Figure 5A,B are collected in Figure 5C using $D_n = d^2/2.35\tau_t$ (d denotes film thickness, $\tau_t = 1/2\pi f_{IMPS}$), which in detail demonstrates the better charge transport in ZnO/QW than ZnO/HJ. Moreover, as the light intensity increases, the diffusion coefficients in ZnO and in QW are both enhanced (see Figure 5C) because of the increased carriers generated with increasing light intensity. The increasing arc span ratio of QW (HJ) to ZnO in IMPS suggests that the

Table 2. EIS Parameters Obtained from the Fitting of Nyquist Plots for the ZnO/HJ and ZnO/QW Solar Cells at 0.8 V Forward Bias

solar cells	R_s (Ω)	R_t (Ω)	R_{CE} (Ω)	R_r (Ω)	C_μ (mF)	L_n (μ m)
ZnO/HJ	9.70 ± 0.4	18.5 ± 0.5	24.0 ± 1.5	51 ± 2	0.50 ± 0.01	41.5
ZnO/QW	11.25 ± 0.4	4.2 ± 0.2	36.0 ± 1.7	105 ± 3	0.58 ± 0.01	125.0

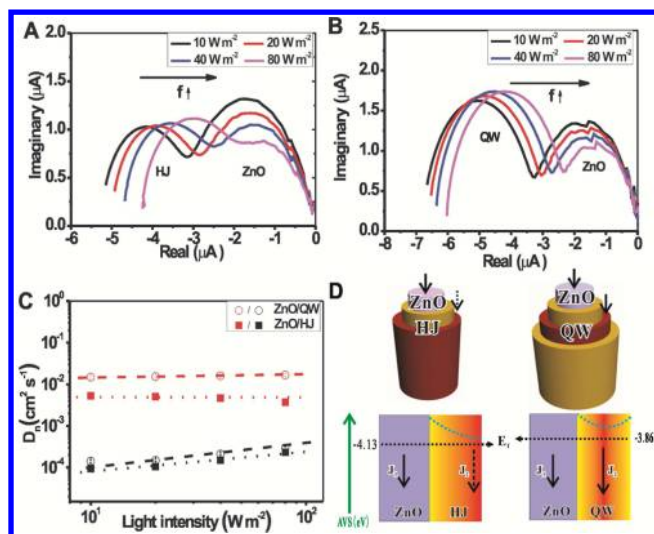


Figure 5. Charge-transport measurement results. IMPS responses of the (A) ZnO/HJ and (B) ZnO/QW solar cells. (C) The extracted diffusion coefficients of HJ, QW, and ZnO from IMPS for the ZnO/HJ and ZnO/QW solar cells. (D) Schematic illustration of the two channel transport model and the proposed energy band diagram of ZnO/HJ and ZnO/QW based on the measured Fermi level (J_2 of HJ flows along the surface whereas J_2 of QW flows along the middle trench).

QW (HJ) channel becomes more and more dominant as the light intensity increases because of the more and more carrier generation in the QW (HJ) channel. The results can be understood by the schematic energy diagrams in Figure 5D for ZnO/QW than ZnO/HJ according to the measured Fermi levels (E_f) and the CB edge profiles of the electrode (details in Figure S2). In Figure 5D, J_1 represents photocurrent along ZnO and J_2 along HJ (QW). Clearly, in HJ, electrons tend to transfer to the outmost CdSe layer due to the much lower CB edge of CdSe than that of ZnSe. Thus the transport in HJ along the outer surface is dragged down by electron trap states due to surface defects or electrolyte redox couples and thus leads to the larger transport resistance and lower J_{sc} (see the left of Figure 5D). In QW, however, due to the energy barrier formed by ZnSe, the electrons are forced to transport in the potential well with a relatively smaller transport resistance and larger recombination resistance, yielding more efficient charge collection and larger J_{sc} (see the right of Figure 5D). Furthermore, the uplifting of the Fermi level from -4.13 eV of ZnO/HJ to -3.86 eV of ZnO/QW also supports the enhanced V_{oc} according to $V_{oc} = (E_f - E_{redox})/q$, where E_{redox} is the energy level of the redox couple and q is the electron charge.⁵⁰

Charge-Transfer Dynamics from ZnO to CdSe. To further investigate the two channel transport mechanism, we now examine charge transfer from ZnO to sensitizers, which may be relevant to the back electron-transfer step in an operating solar cell made by these heterojunction electrodes. Along this line, we pumped electrons from the VB to the CB of ZnO in the core and extracted the ensuing possible charge-transfer dynamic information through TRPL. Actually, this situation is similar to that of an operating solar cell under open circuit condition, and thus the afore-obtained EIS parameters near the open circuit condition can be employed here for the interpretation of the TRPL results.

Figure 6A displays the streak camera images of TRPL, which detailedly map the PL decays at different wavelengths and

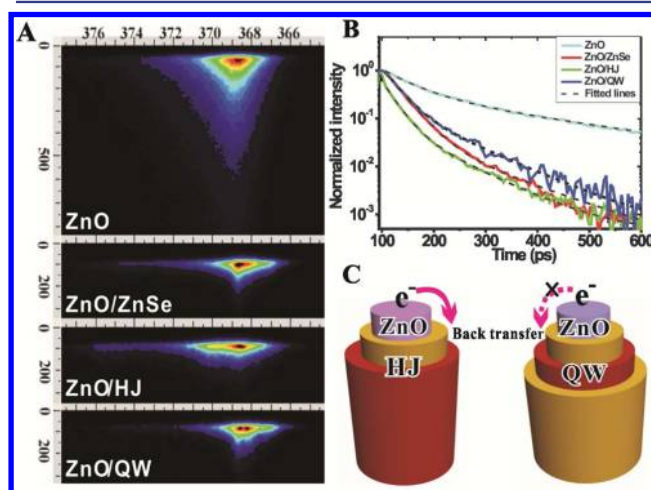


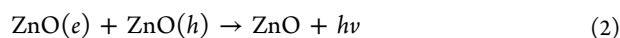
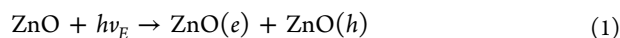
Figure 6. TRPL of the four photoanodes at 17 K. (A) time-resolved PL streak camera images of ZnO, ZnO/ZnSe, ZnO/HJ, and QW-ZnSe for ZnO emission. (B) Fitted TRPL of ZnO emission with biexponential decay traces from the ZnO, ZnO/ZnSe, ZnO/HJ, and ZnO/QW electrodes (ZnO/QW exhibits much faster decay, whereas ZnO/HJ shows slower decay than the reference ZnO/ZnSe photoanode). (C) The schematic illustration of electron-transfer based on the TRPL analysis (ZnO/HJ displays an appreciable electron-transfer rate from ZnO to HJ, whereas ZnO/QW can restrain such electron transfer from ZnO to QW).

provide an overview about the transient spectral behavior derived from the ZnO core. Shown in Figure 6B is a set of PL decay curves of ZnO component extracted from Figure 6A for the four electrodes of ZnO, ZnO/ZnSe, ZnO/HJ, and ZnO/QW. On the basis of the fitted PL decay data with a typical biexponential form, we have quantitatively extracted the decay lifetimes. The two components of the decay curves were then combined to obtain average lifetimes ($\tau_{av} = (A_1\tau_1 + A_2\tau_2)/(A_1 + A_2)$), which are listed in Table 3 for meaningful comparisons.

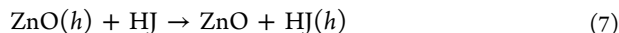
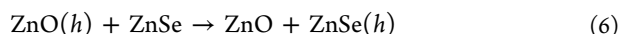
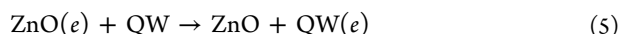
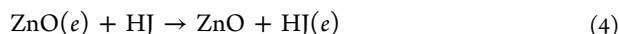
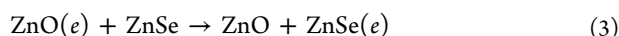
Table 3. PL Decay Times Obtained from the Fitting for the Four Electrodes

electrodes	τ_1 (ps)	A_1	τ_2 (ps)	A_2	τ_{av} (ps)
ZnO	56.2 ± 0.2	4.3	252.3 ± 2.9	0.49	75.8 ± 0.6
ZnO/ZnSe	30.9 ± 0.2	28.2	112.5 ± 5.2	0.13	31.3 ± 0.6
ZnO/HJ	25.0 ± 0.2	54.8	96.9 ± 2.5	0.31	25.4 ± 0.6
ZnO/QW	38.5 ± 0.2	17.7	141.3 ± 6.8	0.15	34.9 ± 0.6

First, compared to the bare ZnO electrode, the remaining three electrodes featuring semiconductor junctions show a much faster PL decay, clearly due to the quenching by the added shells. As a most important observation, with reference to the ZnO/ZnSe electrode, the PL of ZnO/QW exhibits a slower decay but that of ZnO/HJ decays even faster. In all of these electrodes, the PL excitation of ZnO results in electron–hole (e–h) creation (eq 1) followed by recombination of the charge carriers (eq 2):



Charge transfer in these heterojunctions (ZnO/ZnSe, ZnO/HJ and ZnO/QW) (eqs 3–8) can cause quenching of the radiative recombination (eq 2) in the ZnO core, and therefore the charge-transfer kinetics can be captured by difference of their quenching rates.^{52–56}



The fact that ZnSe and CdSe have much higher VB edges than that of ZnO (ZnO: -7.5 eV; ZnSe: -6.1 eV; and CdSe: -6.0 eV; in the absolute vacuum scale) results in a large driving force ($\Delta G = E_{\text{VB-ZnO}} - E_{\text{VB-ZnSe (CdSe)}}$, -1.4 , -1.5 eV) for hole transfer (eqs 6–8). According to the many-state Marcus model,⁵⁶ when $-\Delta G < \lambda$ (system reorganization energy), the charge-transfer rate should exhibit a steep rise with increasing $-\Delta G$, gradually approaching a broad maximum. Therefore, we believe that these three heterojunction electrodes (ZnO/ZnSe, ZnO/HJ, and ZnO/QW) should have similar hole-transfer rates because of the similarly sufficient driving forces.

The apparent hole-transfer rate, approximately expressed as $k_{\text{HT}} = k_{\text{CT}} - k_{\text{ET}}$, can be estimated for the ZnO/ZnSe electrode ($1.88 \times 10^{10} \text{ s}^{-1}$) from the quenching rate difference of this electrode from the bare ZnO electrode expressed by eq 9 by assuming $k_{\text{ET}} = 0$ because the electron-transfer, eq 3, is energetically disfavored owing to the much lower CB edge of ZnO than that of ZnSe. The apparent hole-transfer rates for the three heterostructures are therefore as large as $1.88 \times 10^{10} \text{ s}^{-1}$, which largely account for their PL difference from the aforementioned bare ZnO electrode.

$$k_{\text{HT}} = k_{\text{CT}} = 1/\tau_{\text{av}}(\text{ZnO/ZnSe}) - 1/\tau_{\text{av}}(\text{ZnO}) \quad (9)$$

On the basis of the above analysis, we can use the ZnO/ZnSe electrode as the reference electrode to further estimate the apparent electron-transfer rate from ZnO to CdSe according to eq 10, with the assumption that $k_{\text{ET}} = k_{\text{CT}} - k_{\text{HT}}$ and $k_{\text{CT}} = 1/\tau_{\text{av}}(\text{ZnO/*}) - 1/\tau_{\text{av}}(\text{ZnO})$, (* denotes HJ or QW).

$$k_{\text{ET}} = 1/\tau_{\text{av}}(\text{ZnO/*}) - 1/\tau_{\text{av}}(\text{ZnO/ZnSe}) \quad (10)$$

Interestingly, the k_{ET} of ZnO/HJ from the ZnO core to CdSe shell through the ZnSe layer obtained in this way is as high as $7.4 \times 10^9 \text{ s}^{-1}$, meaning that the electrons in ZnO easily transfer to CdSe, a downhill process. In ZnO/QW, however, k_{ET} become negative ($-3.2 \times 10^9 \text{ s}^{-1}$), which is not unreasonable inasmuch as the electrons in ZnO simply cannot transfer to CdSe in the QW structure.

It is gratifying that the above interpretation of the PL data is consistent with the E_{CB} values estimated from our EIS and UPS results. From the relation $E_{\text{CB}} = E_{\text{f}} - (k_{\text{B}}T/\alpha) \ln C_{\mu}k_{\text{B}}T/e^2$, where k_{B} is the Boltzmann constant; α is the electron-state distribution parameter; T is the temperature; and C_{μ} is the chemical capacitance. From the similar C_{μ} values extracted from EIS (see green oval enclosed in Figure S6, near V_{oc}),⁴⁹ we can see that E_{CB} is solely determined by E_{f} . From the E_{f} values obtained by UPS for four electrodes (see Figure S2, ZnO: -4.38 eV; ZnO/ZnSe: -3.83 eV; ZnO/HJ: -4.13 eV; ZnO/

QW: -3.86 eV), one can find that E_{CB} of QW is 0.27 eV higher than that of HJ and thereby realize why in ZnO/QW electron transfer from ZnO to CdSe is less likely than in ZnO/HJ, in conformity with the slower PL decay of the former than the latter. Consequently, as schematized in Figure 6C, the QW structure permits much more efficient charge collection than the HJ counterpart with the characteristic type II core/shell structure.

Additionally, from the fact of significant electron transfer from ZnO to HJ in ZnO/HJ but still considerable photocurrent in the corresponding solar cell, one is led to the scenario that the sensitizer shell could act as a reasonably efficient electron transport channel, which is in line with the two-channel transport mechanism we proposed above and also in our previous work.³¹ By comparison, the electron transport along QW is much more fluent than along HJ.

Thickness Effects of Core/Shell Heterostructures.

Finally, we have investigated the thickness effects of the quasi-QW structure on the cell performance, which have turned out to be quite revealing of why the QW structure is the best sensitizer among the structures we have studied here. Figure 7A

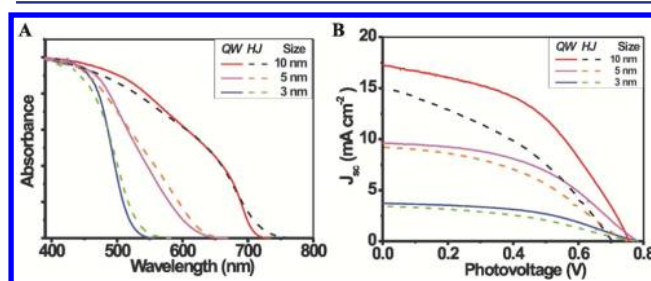


Figure 7. Thickness effects of the CdSe shell on (A) the absorption spectra and (B) the J - V curves for ZnO/QW and ZnO/HJ.

displays the UV-vis absorption spectra of ZnO/HJ and ZnO/QW at three different thicknesses of the CdSe shell (3, 5, 10 nm). As the thickness of CdSe decreases, it can be seen that the absorption edge shifts to the blue for both structures, e.g., the absorption edge shifts from about 710 nm (1.74 eV) for ZnO/QW with a 10 nm thickness of CdSe to 550 nm (2.25 eV) with a 3 nm thickness. Such a thickness effect can be attributed to the quantum size effect, which should have a direct bearing on the PV performance of the corresponding solar cells. Indeed, as shown in Figure 7B, the photovoltage generally increases for both heterostructures as the CdSe shell thickness decreases. This can be understood as resulting from the uplifting of the conduction band edge associated with the CdSe shell thickness reduction, and the consequent alleviation of charge recombination as will be verified below by our TRPL data. However, the overall cell performance actually decreased, because on the other hand, decreasing the CdSe shell thickness in general lowers the photocurrent due to the resulting compromise of the light harvesting capability. Therefore, one has to consider the overall effect of the CdSe thickness on the PV performance. On close examination, one can find that with increasing thickness of the CdSe layer from about 3 to 10 nm, the V_{oc} obtained in ZnO/QW dropped much less than that of ZnO/HJ, counter to the much larger photocurrent increase of the former than of the latter. Therefore, the ZnO/QW structure is clearly more advantageous in achieving both high J_{sc} and high V_{oc} than the ZnO/HJ. In addition, this study also raises the possibility of using multiple ultrathin CdSe shells separated by the alternating

ZnSe shells, that is, multiple QWs, because such architecture could preserve the high photovoltage without compromising the photocurrent.

More detailed studies on how the thicknesses of the ZnSe and CdSe shells influence the electron-transfer dynamics in the heterostructures have been performed with TRPL. The result is shown in Figure 8. One can see from Figure 8A,C that

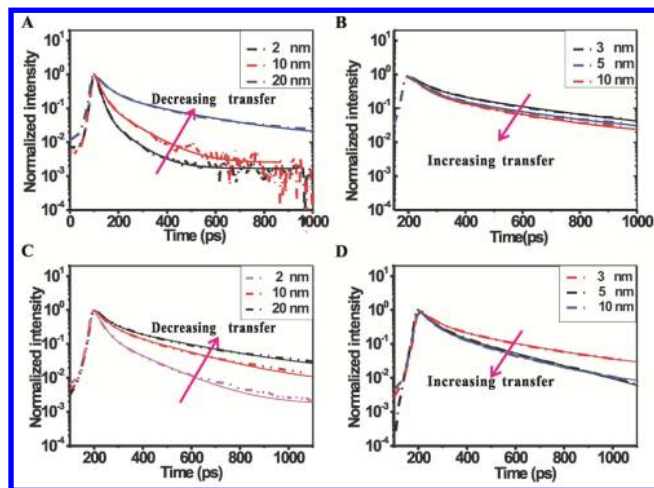


Figure 8. Thickness effects of the first-layer ZnSe and second-layer CdSe shells on TRPL spectra. (A) The increasing ZnSe thickness leads to decreasing electron-transfer rate from ZnO to HJ (10 nm CdSe), but (B) the increasing CdSe thickness results in increasing electron-transfer rate from ZnO to HJ (20 nm ZnSe). (C) The increasing ZnSe thickness of inner layer leads to decreasing electron-transfer rate from ZnO to QW (10 nm CdSe), but (D) the increasing CdSe thickness results in increasing electron-transfer rate from ZnO to QW (10 nm ZnSe).

increasing the ZnSe shell thickness generally decreases the electron-transfer rates from ZnO to HJ and to QW, and about 20 nm thick ZnSe in ZnO/HJ and 10 nm thick ZnSe in ZnO/QW could fully suppress the electron transfer, consistent with the role of the ZnSe shell as a barrier layer employed in this study. In contrast, increasing the CdSe thickness generally increases the electron-transfer rates from ZnO to HJ and to QW, as shown in Figure 8B,D, respectively. This nicely confirms the explanation given above on the increased photovoltage as a consequence of decreasing the CdSe thickness. In a nutshell, the decreased CdSe shell thickness should uplift the CB edge stemming from the quantum size effect, hinder the electron transfer from ZnO to HJ (or QW), which is essentially the charge recombination step in our solar cells in operation, and thereby boost the photovoltage.

CONCLUSION

We have demonstrated a new QW structure (ZnSe/CdSe/ZnSe tube) as the sensitizer for photoelectrochemical solar cells and achieved about 6.20% PCE, which is considerably higher than the ZnO/HJ control cell (4.01%) and indeed among the highest reported to date for such SSSCs. The electrochemical impedance studies have revealed that the QW structure (ZnO/QW) has one-fourth the transport resistance but twice the recombination resistance of the ZnO/HJ structure, yielding twice longer electron diffusion length, consistent with the resulting higher V_{oc} , J_{sc} , FF, and consequently the higher PCE than the control ZnO/HJ solar cell. The TRPL data have

supported the superior charge separation and collection in ZnO/QW to that in ZnO/HJ. Moreover, the two-channel transport mechanism in the QW-sensitized solar cells has been proposed and supported by the improved charge transport from HJ to QW revealed by EIS, the two IMPS responses, and the TRPL results, opening up a new avenue for the development of SSSCs.

EXPERIMENTAL SECTION

Synthesis of ZnO Tetrapods and Nanorod Arrays. ZnO tetrapods were synthesized through metal vapor transport and oxidation technique as our previous work. We employed 1 g of Zn strands source and 50/200 O_2/N_2 standard cubic centimeters per minute in this work, yielding 50–200 nm diameter, 400–1000 nm length nano tetrapod-like rods. For ZnO nanorod arrays synthesis, zinc acetate dehydrates and ethanolamine as starting materials for seeds. Five mM solution was spin coated on FTO substrate and annealed at 350 °C. The FTO was put into a mixture solution of 25 mM zinc nitride and 25 mM hexamethylenetetramine and heat to 92 °C for 4 h.

Photoanode Preparation. 0.5 g tetrapods were dispersed in 6 mL 10% ethyl cellulose of terpineol at 80 °C without continuous stirring. Then the doctor blade technique was employed to obtain about 20 μ m thick on the nanorod array covered FTO. The quasi-QWs of ZnSe/CdSe/ZnSe were prepared by successively dip coating. First, ZnO tetrapods placed in a Se^{2-} ion solution (2.0 mM) prepared by reacting Se powder with $NaBH_4$ and kept at 50 °C under N_2 purging for 0.1–6 h to produce 2–20 nm ZnSe shell through ion exchange. ZnO/ZnSe core/shell tetrapods films were rinsed with water and then placed in 5 mM $CdCl_2$ solution to partially exchange the Zn^{2+} with Cd^{2+} ions at 50 °C under N_2 purging for 4 h. Then alternatively placed it in freshly prepared Se^{2-} and Cd^{2+} solutions for several times to get a desirable thickness of CdSe. Finally, ZnO/ZnSe/CdSe was further dipped in 5 mM Zn^{2+} and Se^{2-} alternatively for 2 h to produce the final ZnSe (repeat this cycle twice). Afterward, ZnS shells were coated by successively twice dip coating of Zn^{2+} and S^{2-} on ZnO/ZnSe/CdSe/ZnSe tetrapods for 1 min each. Following each dipping, the films were rinsed for 1 min or more using pure ethanol or water to remove excess precursor.

Solar Cell Fabrication and Characterization. The photoanodes were assembled into solar cells with Pt-sputtered FTO counter electrodes and polysulfide electrolyte containing 1 M Na_2S and 0.25 M S gelled by 0.75 g polyethylene glycol (PEG) 2000000 by using a 60 μ m thick adhesive tape (Scotch brand). The gel electrolyte was employed to improve the performance stability of the cells. The light source (Oriel solar simulator, 450 W Xe lamp, AM 1.5 global filter) was calibrated to 1 sun (100 $mW\ cm^{-2}$) using an optical power meter (Newport, model 1916-C) equipped with a Newport 818P thermopile detector. $J-V$ characteristic curves and intensity modulated photocurrent/photovoltage spectroscopy (IMPS/IMVS) were measured by the Zahner controlled intensity modulated photoresponse spectroscopy (C-IMPS) system. Incident photon to current conversion efficiencies (IPCEs) was measured on photo current spectra system of CIMPS (CIMPS-PCS) with tunable light source (TLS03). The photoanode film area for the QDSSCs and DSSCs performance test was typically 0.25 cm^2 using a black paint coated Al foil as a mask. Morphologies of the nanomaterials and subsequent nanostructures were directly examined on JEOL6700F SEM at an accelerating voltage of 5 kV. TEM observations were carried out on a JEOL 2010F microscope operating at 200 kV. Diffused reflectance spectra were carried out on the same film samples using a Perkin-Elmer UV–vis spectrophotometer (model Lambda 20). The film thickness was determined by a Tencor Alpha-Step 200 surface profiler system. Raman measurements were conducted with a Renishaw 2000 laser Raman microscope equipped with a 514.5 nm 20 mW argon ion laser of 2 mm spot size for excitation. The valence band structures were determined by ultraviolet photoemission spectroscopy in Kratos Axis Ultra DLD multitechnique surface analysis system. For TRPL measurements, a tunable Ti:sapphire femtosecond-pulsed laser was used as the excitation light source, with the excitation wavelength 266

nm and the incident light intensity was 1 W cm^{-2} . A Hamamatsu C5680-04 streak camera was used for TRPL. An APD Cryogenics system (model EXPPANDER DE202) was used to cool down the sample, and the TRPL measurement was taken at its lowest temperature 17 K.

■ ASSOCIATED CONTENT

● Supporting Information

HRTEM images of ZnO, ZnO/ZnSe, ZnO/HJ, and ZnO/QW, UPS data for the four electrodes, Raman spectroscopy of the photoanodes: pure ZnO, ZnO/HJ, and ZnO/QW, J - V curves using Pt counter electrode, impedance spectra between GO/Cu₂S and Pt counter electrode at open circuit, J - V curve of ZnO/ZnSe electrode and chemical capacitance curves extracted from EIS measurement. This material is available free of charge via the Internet at <http://pubs.acs.org>.

■ AUTHOR INFORMATION

Corresponding Author

chsyang@ust.hk

Notes

The authors declare no competing financial interest.

■ ACKNOWLEDGMENTS

This work was supported by the HK-RGC General Research Funds (GRF No. HKUST 606511, 605710 and 604410).

■ REFERENCES

- (1) Norris, D. J.; Bawendi, M. G. *Phys. Rev. B* **1996**, *53*, 16338–16346.
- (2) Yu, W. W.; Qu, L. H.; Guo, W. Z.; Peng, X. G. *Chem. Mater.* **2003**, *15*, 2854–2860.
- (3) Pandey, A.; Guyot-Sionnest, P. *Science* **2008**, *322*, 929–932.
- (4) Tisdale, W. A.; Williams, K. J.; Timp, B. A.; Norris, D. J.; Aydil, E. S.; Zhu, X. Y. *Science* **2010**, *328*, 1543–1547.
- (5) Chan, W. L.; Ligges, M.; Jilaubekov, A.; Kaake, L.; Miaja-Avila, L.; Zhu, X. Y. *Science* **2011**, *334*, 1541–1545.
- (6) Zhu, H. M.; Lian, T. Q. *J. Am. Chem. Soc.* **2012**, *134*, 11289–11297.
- (7) Yang, Y.; Rodriguez-Cordoba, W.; Xiang, X.; Lian, T. Q. *Nano Lett.* **2012**, *12*, 303–309.
- (8) Pandey, A.; Guyot-Sionnest, P. *J. Phys. Chem. Lett.* **2010**, *1*, 45–47.
- (9) Kamat, P. V. *Nat. Chem.* **2010**, *2*, 809–810.
- (10) Liu, S.; Borys, N. J.; Huang, J.; Talapin, D. V.; Lupton, J. M. *Phys. Rev. B* **2012**, *86*, 045303.
- (11) Shabaev, A.; Efros, A. L.; Nozik, A. J. *Nano Lett.* **2006**, *6*, 2856–2863.
- (12) Sitt, A.; Della Sala, F.; Menagen, G.; Banin, U. *Nano Lett.* **2009**, *9*, 3470–3476.
- (13) Fisher, B.; Caruge, J. M.; Zehnder, D.; Bawendi, M. *Phys. Rev. Lett.* **2005**, *94*, 087403.
- (14) Franceschetti, A.; Zhang, Y. *Phys. Rev. Lett.* **2008**, *100*, 136805.
- (15) Lim, C. S.; Im, S. H.; Rhee, J. H.; Lee, Y. H.; Kim, H. J.; Maiti, N.; Kang, Y.; Chang, J. A.; Nazeeruddin, M. K.; Gratzel, M.; Seok, S. I. *J. Mater. Chem.* **2012**, *22*, 1107–1111.
- (16) Chang, J. A.; Rhee, J. H.; Im, S. H.; Lee, Y. H.; Kim, H. J.; Seok, S. I.; Nazeeruddin, M. K.; Gratzel, M. *Nano Lett.* **2010**, *10*, 2609–2612.
- (17) Chang, J. A.; Im, S. H.; Lee, Y. H.; Kim, H. J.; Lim, C. S.; Heo, J. H.; Seok, S. I. *Nano Lett.* **2012**, *12*, 1863–1867.
- (18) Boix, P. P.; Larramona, G.; Jacob, A.; Delatouche, B.; Mora-Sero, I.; Bisquert, J. *J. Phys. Chem. C* **2012**, *116*, 1579–1587.
- (19) Itzhak, Y.; Niitsoo, O.; Page, M.; Hodes, G. *J. Phys. Chem. C* **2009**, *113*, 4254–4256.
- (20) Moon, S. J.; Itzhak, Y.; Yum, J. H.; Zakeeruddin, S. M.; Hodes, G.; Gratzel, M. *J. Phys. Chem. Lett.* **2010**, *1*, 1524–1527.
- (21) Im, S. H.; Kim, H. J.; Rhee, J. H.; Lim, C. S.; Sang, S. I. *Energy Environ. Sci.* **2011**, *4*, 2799–2802.
- (22) Lim, C. S.; Im, S. H.; Kim, H. J.; Chang, J. A.; Lee, Y. H.; Seok, S. I. *Phys. Chem. Chem. Phys.* **2012**, *14*, 3622–3626.
- (23) Kim, H. S.; Lee, C. R.; Im, J. H.; Lee, K. B.; Moehl, T.; Marchioro, A.; Moon, S. J.; Humphry-Baker, R.; Yum, J. H.; Moser, J. E.; Gratzel, M.; Park, N. G. *Sci. Rep.* **2012**, *2*, 591.
- (24) Lee, M. M.; Teuscher, J.; Miyasaka, T.; Murakami, T. N.; Snaith, H. J. *Science* **2012**, *338*, 643–647.
- (25) Noh, J. H.; Im, S. H.; Heo, J. H.; Mandal, T. N.; Seok, S. I. *Nano Lett.* **2013**, *13*, 1764–1769.
- (26) Qiu, J. H.; Qiu, Y. C.; Yan, K. Y.; Zhong, M.; Mu, C.; Yan, H.; Yang, S. H. *Nanoscale* **2013**, *5*, 3245–3248.
- (27) Santra, P. K.; Kamat, P. V. *J. Am. Chem. Soc.* **2012**, *134*, 2508–2511.
- (28) Hossain, M. A.; Jennings, J. R.; Shen, C.; Pan, J. H.; Koh, Z. Y.; Mathews, N.; Wang, Q. *J. Mater. Chem.* **2012**, *22*, 16235–16242.
- (29) Mora-Sero, I.; Bisquert, J. *J. Phys. Chem. Lett.* **2010**, *1*, 3046–3052.
- (30) Zhang, Q. X.; Guo, X. Z.; Huang, X. M.; Huang, S. Q.; Li, D. M.; Luo, Y. H.; Shen, Q.; Toyoda, T.; Meng, Q. B. *Phys. Chem. Chem. Phys.* **2011**, *13*, 4659–4667.
- (31) Yan, K. Y.; Chen, W.; Yang, S. H. *J. Phys. Chem. C* **2013**, *117*, 92–99.
- (32) Hossain, M. A.; Jennings, J. R.; Mathews, N.; Wang, Q. *Phys. Chem. Chem. Phys.* **2012**, *14*, 7154–7161.
- (33) Yu, X. Y.; Liao, J. Y.; Qiu, K. Q.; Kuang, D. B.; Su, C. Y. *ACS Nano* **2011**, *5*, 9494–9500.
- (34) Huang, S. Q.; Zhang, Q. X.; Huang, X. M.; Guo, X. Z.; Deng, M. H.; Li, D. M.; Luo, Y. H.; Shen, Q.; Toyoda, T.; Meng, Q. B. *Nanotechnology* **2010**, *21*, 375201.
- (35) Lee, Y. L.; Lo, Y. S. *Adv. Funct. Mater.* **2009**, *19*, 604–609.
- (36) Choi, H.; Nicolaescu, R.; Paek, S.; Ko, J.; Kamat, P. V. *ACS Nano* **2011**, *5*, 9238–9245.
- (37) Buhbut, S.; Itzhakov, S.; Oron, D.; Zaban, A. *J. Phys. Chem. Lett.* **2011**, *2*, 1917–1924.
- (38) Ning, Z. J.; Yuan, C. Z.; Tian, H. N.; Hedstrom, P.; Sun, L. C.; Agren, H. *ChemSusChem* **2011**, *4*, 1741–1744.
- (39) Salant, A.; Shalom, M.; Tachan, Z.; Buhbut, S.; Zaban, A.; Banin, U. *Nano Lett.* **2012**, *12*, 2095–2100.
- (40) Nabetani, Y.; Kato, T.; Matsumoto, T. *J. Appl. Phys.* **2001**, *89*, 154–159.
- (41) Nabetani, Y.; Kato, T.; Matsumoto, T. *J. Cryst. Growth* **2000**, *214*, 610–615.
- (42) Yang, F.; Hayes, G. R.; Phillips, R. T.; O'Donnell, K. P. *Phys. Rev. B* **1996**, *53*, R1697–R1700.
- (43) Rosenauer, A.; Reisinger, T.; Steinkirchner, E.; Zweck, J.; Gebhardt, W. *J. Cryst. Growth* **1995**, *152*, 42–50.
- (44) Yamaguchi, S.; Kawakami, Y.; Fujita, S.; Yamada, Y.; Mishina, T.; Masumoto, Y. *Phys. Rev. B* **1996**, *54*, 2629–2634.
- (45) Afshar, M.; Sadewasser, S.; Albert, J.; Lehmann, S.; Abou-Ras, D.; Marron, D. F.; Rockett, A. A.; Rasanen, E.; Lux-Steiner, M. C. *Adv. Energy Mater.* **2011**, *1*, 1109–1115.
- (46) Xu, J.; Yang, X.; Wang, H. K.; Chen, X.; Luan, C. Y.; Xu, Z. X.; Lu, Z. Z.; Roy, V. A. L.; Zhang, W. J.; Lee, C. S. *Nano Lett.* **2011**, *11*, 4138–4143.
- (47) Xu, J.; Yang, X.; Yang, Q. D.; Wong, T. L.; Lee, S. T.; Zhang, W. J.; Lee, C. S. *J. Mater. Chem.* **2012**, *22*, 13374–13379.
- (48) Wang, K.; Chen, J. J.; Zhou, W. L.; Zhang, Y.; Yan, Y. F.; Pern, J.; Mascarenhas, A. *Adv. Mater.* **2008**, *20*, 3248–3253.
- (49) Radich, J. G.; Dwyer, R.; Kamat, P. V. *J. Phys. Chem. Lett.* **2011**, *2*, 2453–2460.
- (50) Fabregat-Santiago, F.; Garcia-Belmonte, G.; Mora-Sero, I.; Bisquert, J. *Phys. Chem. Chem. Phys.* **2011**, *13*, 9083–9118.
- (51) Yan, K. Y.; Qiu, Y. C.; Chen, W.; Zhang, M.; Yang, S. H. *Energy Environ. Sci.* **2011**, *4*, 2168–2176.

- (52) Kongkanand, A.; Tvrđy, K.; Takechi, K.; Kuno, M.; Kamat, P. V. *J. Am. Chem. Soc.* **2008**, *130*, 4007–4015.
- (53) Farrow, B.; Kamat, P. V. *J. Am. Chem. Soc.* **2009**, *131*, 11124–11131.
- (54) Bang, J. H.; Kamat, P. V. *Adv. Funct. Mater.* **2010**, *20*, 1970–1976.
- (55) Lightcap, I. V.; Kamat, P. V. *J. Am. Chem. Soc.* **2012**, *134*, 7109–7116.
- (56) Tvrđy, K.; Frantsuzov, P. A.; Kamat, P. V. *Proc. Natl. Acad. Sci. U.S.A.* **2011**, *108*, 29–34.